Journal of Applied Research and Technology

www.jart.icat.unam.mx

Journal of Applied Research and Technology 23 (2025) 579-593

Original

Micrometric Probe and Sample Position Measurement in Scanning Probe Microscopy Through Computer Vision

J. L. Martínez-Valencia[1] • J. Castillo-Hernández
G. A. Holguín-Londoño[2], D. Matatagui,
M. Holguín-Londoño[2] • C.L. Ordoñez-Romero[4] and N. Qureshi[1]

[1]Instituto de Ciencias Aplicadas y Tecnología, Universidad Nacional Autónoma de México, Ciudad Universitaria, Coyoacán, Mexico City 04510, Mexico
[2]Facultad de Ingenierías, Universidad Tecnológica de Pereira, Pereira, Risaralda 660001, Colombia
[3]Instituto de Magnetismo Aplicado, Universidad Complutense de Madrid, Las Rozas de Madrid 28232, Spain
[4]Instituto de Física, Universidad Nacional Autónoma de México, Ciudad Universitaria, Coyoacán, Mexico City 04510, Mexico

Received: 05 31 2024; Accepted: 02 22 2025
Available: 12 31 2025

Abstract: This work presents a computer vision-based methodology for precise, dynamic probe-sample distance measurement in scanning probe microscopy. The technique is tested by scanning a representative planar microwave probe and monitoring its position in three dimensions using a stereoscopic optical microscope. The results demonstrate that, through triangulation, the spatial resolution of the three-dimensional system surpasses that of the individual optical microscopes. This paper also introduces an approach that addresses the challenges of camera calibration and the limited number of feature matches between images, using augmented reality tags (ARTags) and Kalman filters to ensure process continuity and robustness. A notable feature of the methodology is its ability to estimate distances without relying on specific sample characteristics or direct contact with the sample surface. The proposed algorithms are scalable, allowing for the generation of partial or complete reconstructions of micrometric

*Corresponding author.
E-mail address: naser.qureshi@icat.unam.mx (N. Qureshi).
Peer Review under the responsibility of Universidad Nacional Autónoma de México.

three-dimensional scenes. This facilitates control of the tip-sample distance and could enable more advanced real-time route planning in scanning probe microscopy.

Keywords: **computer vision, scanning probe microscopy, microwave microscope, augmented reality.**

1. Introduction

Scanning probe microscopy (SPM) encompasses a diverse range of techniques united by the common approach of scanning a sample with a probe to generate high-resolution images. These techniques enable the visualization of diverse sample properties by quantifying probe-sample interactions. Prominent examples include atomic force microscopy (AFM) and scanning tunneling microscopy (STM), which emerged in the 1980s (Tabib-Azar et al., 1993; Golosovsky & Davidov,1996; Vlahacos et al., 1996). Scanning microwave microscopy (SMM) (Synge, 1928; Ash & Nicholls, 1972) uses near-field microwave radiation confined to small volumes at micrometer- and nanometer-length scales. Microwaves can penetrate numerous materials, facilitating the characterization of both surface and subsurface properties (Siegel, 2021). However, meticulous control over the distance between the probe and the sample is imperative to extract sample properties successfully (Siegel, 2021). This is because tip-sample coupling in the near field decreases strongly with distance. Therefore, precise control at the micrometer scale is indispensable.

The electromagnetic interaction between the probe and the sample yields additional information, often in the form of a recorded reflection coefficient, which is instrumental in investigating the sample's microwave-frequency characteristics. Properties of interest include the dielectric constant, resistivity, and dispersion. Such characterization holds considerable utility in contemporary nanomaterials and nanoparticle research (Farina et al., 2017). Furthermore, its potential extends to the characterization of ferroelectric and dielectric materials (Feenstra et al., 1998; Yoo et al., 2001) and biological samples (Wang et al., 2000).

In recent years, significant strides have been made in microwave microscopy research, motivated by its merits as a non-contact, non-destructive technique that delivers remarkable spatial resolution (Imtiaz et al., 2014; Hu et al., 2006). Nonetheless, the intricate interplay between microwave sources, probes, and samples, as well as the interaction between the receiver and the underlying transmission line, constitutes a profoundly complex challenge (Tang et al., 2021).

The challenges related to positioning have been effectively addressed by the atomic force microscopy (AFM) and scanning tunneling microscopy (STM) communities. In AFM instruments, the movement of a tip in contact with the sample surface deflects a laser, whose deflection greatly amplifies the tip's movement (Lee et al., 2010). This technique, however, involves direct contact between the probe and the sample, which is not desirable in microwave microscopy.

In STM instruments, the amplitude of the tunneling current exhibits remarkable sensitivity to the distance between the tip and the sample at nanometer length scales. This property makes it possible to maintain a constant tip-sample distance through an appropriate feedback loop (Imtiaz et al., 2014). Nevertheless, when dealing with non-conductive samples, applying a current through the sample or relying on its conductivity becomes impractical. Precisely positioning a scanning probe at a constant distance from a sample while scanning over a complex topography, without contact, is an important problem. A similar problem has been addressed in the field of computer microvision—specifically in micromanipulation applications—supplemented by visual feedback (Chang et al., 2018; Masuda et al., 2018).

Over the last two decades, micromanipulation has been used extensively in microelectromechanical systems (MEMS), bioengineering, and the fabrication of microdevices (Sha et al., 2019).

Micromanipulation and microassembly techniques are used in fields such as biological engineering, microdevice processing, medical engineering, and other domains that require intricate operations (Kim et al., 2017). These techniques are especially relevant in the context of MEMS (microelectromechanical systems) (Maroufi et al., 2017; Tng et al., 2012), MOEMS (micro-optoelectromechanical systems) (Lu et al., 2017), BioMEMS (biological

microelectromechanical systems) (Martinez-Rivas et al., 2017; Race et al., 2017; Jeong et al., 2017; Pan et al., 2017), and similar microsystems.

Microvision, as a non-contact, high-precision technique, serves as a real-time monitoring tool for microdevice dynamics, measuring both position and motion, and is an essential part of micromanipulation systems. It involves the integration of multiple data streams into a cohesive package. This integrated framework is aptly called the microvision system (Yu et al., 2017; Fatikow et al., 2008; Guo et al., 2005; Zhao et al., 2018). However, challenges persist within computerized microvision systems, including issues such as system calibration, autofocus, extraction of depth information, and visual micro servo control of robotic platforms (Sha et al., 2019).

In this work, we apply microvision techniques from the field of micromanipulation to a scanning microwave probe system and quantify the precision with which the position of a probe relative to a sample can be measured within a more complex mechanical system. A stereoscopic vision system comprising two microscopes and augmented reality tags (ARTags) is used to digitally recreate a probe-sample scene and then measure the probe-sample distance.

In Sections 2 and 3, we describe our proposed approach to computer vision and include implementation details to facilitate its reproduction. Sections 4 and 5 present an experimental validation of this method, detailing the development process, the materials employed, and the characterization of its performance.

2. Terminology and Assumptions

2.1. Stereoscopic Vision

Considering that scanning microwave microscopes typically use XYZ platforms to achieve spatial scanning over a sample, and given that a sample's topography (or height) can vary irregularly, the challenge of measuring the distance between the probe and the sample can be addressed through a process of optical triangulation (Hügli & Mure-Dubois, 2006).

Stereoscopic vision involves the simultaneous acquisition of two images, captured from distinct viewpoints. In stereomicroscopy, each objective lens provides a separate viewpoint. In machine vision, video sensors are attached to the microscopes. Image-matching algorithms are employed to compute the disparity between the image pair, enabling the reconstruction of three-dimensional (3D) information. Leveraging prior knowledge about the object's geometry can accelerate the matching process.

2.2. Computer Vision for Micrometer Distance Measurement: Projective Geometry

To obtain greater precision in measuring the distance between objects in a scene, it is necessary to consider more than one photograph that observes the scene from another nearby perspective. By capturing several images of the same scene with displaced cameras, a greater amount of information can be acquired to recreate the perception of depth and determine distances between objects in the photograph that cannot be accurately determined with a single photograph. This is the objective of stereoscopic vision (Hartley & Zisserman 2003).

Traditionally, stereovision analysis has been divided into two distinct problems: the correspondence problem and the reconstruction problem. Starting with two two-dimensional images, denoted as I and D, in the coordinate space (u, v), the correspondence problem aims to identify two points, one in image I, and one in image D, that correspond to the same point M in three-dimensional space (X, Y, Z). Once these two points are identified, the reconstruction problem involves determining the coordinates of point M. The most challenging aspect lies in solving the correspondence problem. In general, there are several possible choices for matching an element in image D to an element in image I, which introduces ambiguity into the stereo correspondence problem. Due to this ambiguity, it becomes necessary to determine which elements, characteristics, constraints, and considerations can be applied to minimize it as much as possible (Cyganek & Siebert 2011).

Extracting the three-dimensional structure of a scene from stereoscopic images is a problem that has been extensively studied by the computer-vision community in recent decades. The initial efforts focused on establishing the fundamentals of image correspondence and stereoscopic geometry (Cyganek & Siebert 2011). Over time, research in this field has matured significantly, leading to numerous advances in computational stereo vision. These advances have expanded the application of stereoscopy to new domains, including micrometric microscopy.

3. A Method for Micrometric Distance Estimation of a Scanning Microwave Probe

Here, we consider scanning probe microscopes (SPMs) in which the test probe does not make direct contact with the analyzed sample. A typical scanning microwave microscope (SMM) (Tabib-Azar et al., 1993) can be integrated into the general visual-servo-control process, as shown

geometrically in Figure 1 and schematically in Figure 2. However, when working with microscopy scenes, it becomes necessary to modify each of the subprocesses. For instance, the camera-calibration process, depending on the chosen method, requires the generation of microscopic patterns. Concerning the autofocus thread, although numerous solutions have been proposed in the literature (Hügli & Mure-Dubois, 2006), they are often associated with complex video capture systems. In other words, most microscopes—particularly the readily available ones—lack autofocus, and manual mechanical focusing is typically required.

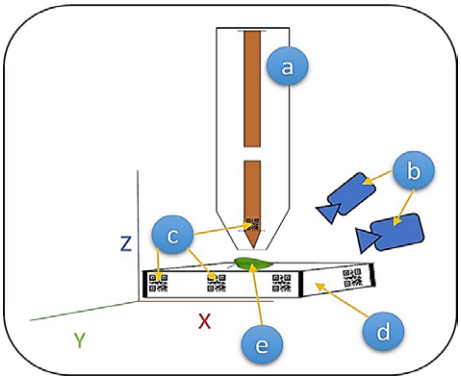

Figure 1. A microwave scanning probe monitored with optical microscopes: a) a representative planar resonant microwave scanning probe moves in three dimensions relative to a sample holder; b) two cameras, each fitted with a low-magnification optical microscope, are pointed at the probe and sample at different angles; c) the scanning probe and the sample holder are marked with millimeter-scale ARTag-coded markers; d) the sample holder is itself a three-dimensional rectangular structure of known dimensions; and e) a nonplanar sample is placed on the sample holder.

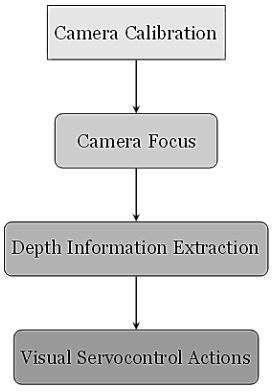

Figure 2. The general process of visual-servo control. This is implemented in a time-efficient manner so that the position of the scanning probe is controlled dynamically during the process of mechanically scanning the sample with a probe.

The most significant challenge lies in the depth of information extraction subsystem. The majority of depth information extraction algorithms are based on identifying corresponding points between images.

However, in microscopic scenes, where image content lacks texture richness, this process becomes challenging, and error margins tend to be high, significantly impacting the results.

Considering the various approaches required for interventions and modifications to the mechanical structure of a scanning microwave microscope, as well as the subprocesses of a visual-servo-control system for microscopic scenes, we propose a method that facilitates the integration of these approaches. The proposed method is summarized in the flowchart depicted in Figure 3 and can be divided into the following four steps, aligning with the general structure of visual-servo-control processes presented in Figure 2:

Step 1: Focusing and calibration of optical microscopes. Utilize established techniques from literature and employ specially designed micrometric augmented reality markers (ARTags) tailored for this application to achieve camera (microscope) focus and calibration.

Step 2: Digital processing of the images and calculation of the projective camera matrices of each of the microscopes.

Step 3: Triangulation of coincident points, partial reconstruction of the three-dimensional scene, and estimation of the microscopy probe location.

Step 4: Servo-control actions on a XYZ axial microstepping system.

3.1 Step 1 — Focusing and Calibration of Optical Microscopes

A manual focusing method is established, in which, with the help of ARTags, the focus quality on the objects of interest is visually identified.

The one proposed in Ref. (Zhang, 2002) was used as the base calibration method. This technique, developed by Zhang, is widely recognized for its flexibility in camera calibration. It relies on the use of multiple images of a planar pattern, such as a chessboard, captured from different angles. By extracting corresponding points between the pattern and the images, the method enables accurate estimation of both intrinsic and extrinsic camera parameters, including lens distortion. This approach is particularly well-suited for situations where high precision is required, such as microscopy, as it accommodates variations in image perspective and distortion introduced by lenses. For our implementation, we adapted

this method by using ARTags as the calibration pattern, which provides robust reference points for camera matrix extraction and distortion correction.

The camera-calibration process, adjusted to microscopic images, can be summarized in the following steps:
(i) Print microscopic ARTag-type patterns on a planar surface.
(ii) Capture multiple images of the pattern with each microscope, ensuring variations in image orientation and perspective.
(iii) Detect the characteristic points of the patterns in each image.
(iv) Estimate the five intrinsic and extrinsic camera parameters using the method proposed in [34].
(v) Refine all parameters, including lens distortion parameters.

Figure 4 shows a series of ARTag-type patterns developed for the calibration process. Each label features a four-bit encoding for identification and an additional bit to determine orientation.

The camera calibration step is executed only once at the inception of the visual-servo-control system. It is unnecessary to repeat this step in subsequent iterations unless there are significant changes in the position, focus, or perspective parameters of the microscopes relative to the scene. We assume that the position and focus of the optical microscopes with respect to the scene remain stable during the data acquisition process.

3.2 Step 2 — Digital Image Processing and Depth-Information Extraction

After achieving focus in the optical microscopes and completing the camera-calibration process, the system begins with image capture of the target scene. To enhance the estimation process, ARTag labels were employed, providing reference points within the scene. We designed 4-bit labels that not only convey their identity but also indicate their orientation within the plane they occupy. These labels have specific dimensions, shapes, and orientations, along with strategic placements. One label is affixed to the tip of the microwave microscopy probe, while others are positioned on the sample base. This setup enables the identification of planes, their size relationships, and the angular differences between them.

Algorithm 1 summarizes the digital image-processing techniques employed to identify and decode the tags in the images, thereby generating a collection of ordered coordinates that serve as robust correspondence across the processed image set.

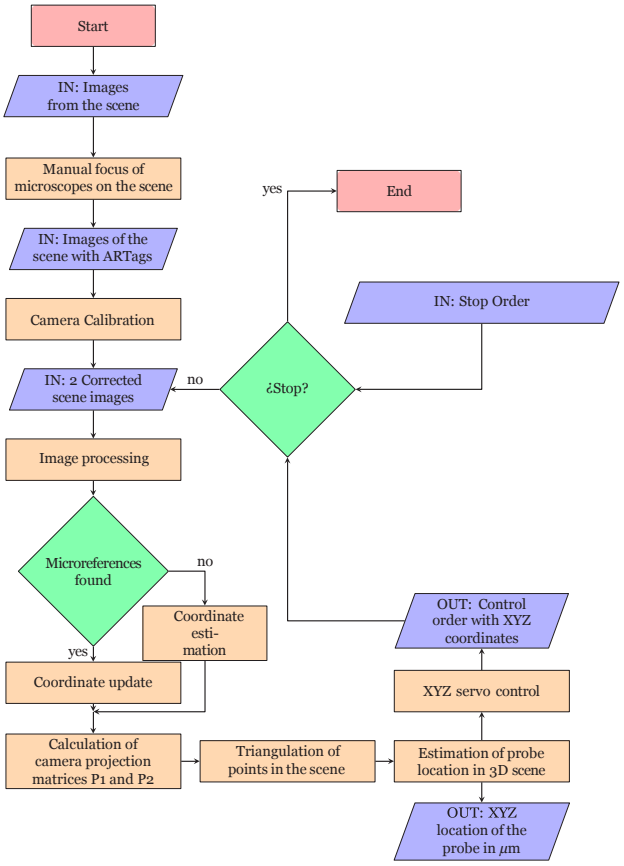

Figure 3. Flowchart for the proposed method for acquiring and processing optical images to produce a digital model of the scene with precisely calibrated dimensions and locations of the probe and sample surfaces.

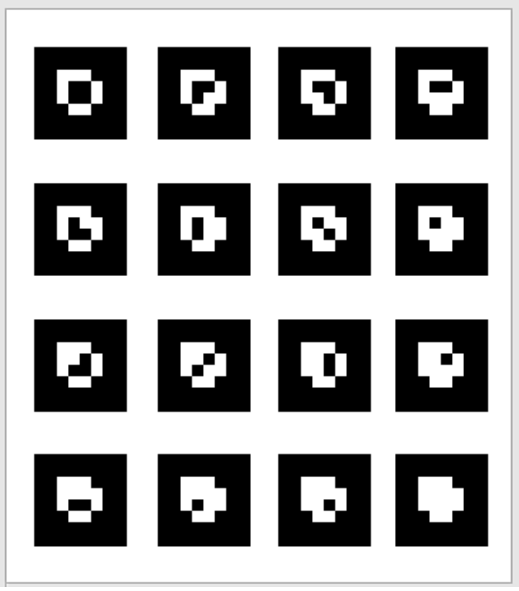

Figure 4. ARTags placed at known positions on the probe and sample for the calibration of optical microscopes.

The digital image-processing algorithm is designed to identify and extract ARTags from images of the scene, leveraging well-established techniques such as Gaussian blurring and Canny edge detection. These methods were selected for their robustness in handling noisy images and their effectiveness in contour detection. The implementation of the Canny edge detection algorithm ensures precise boundary identification, which is crucial for detecting the ARTags that serve as micro-references in the scene.

Initially, Gaussian blurring is applied to reduce noise and smooth the image, facilitating the edge-detection process so as to focus on significant contours. Following edge detection, the algorithm identifies contours with four vertices, corresponding to the rectangular shape of the ARTags. The warp perspective method is then utilized to transform the detected contour into a top-down view, enabling accurate decoding of the ARTag's ID and orientation. The parameters for Gaussian blurring and edge detection are carefully selected based on the scale of the scene and the resolution of the microscopes. Specifically, a moderate Gaussian kernel is employed to balance noise reduction and edge preservation, while the Canny algorithm's thresholds are fine-tuned to enhance sensitivity to the fine features of the ARTags. This parameter optimization ensures that even small tags can be reliably identified.

Ultimately, the algorithm outputs a set of ordered coordinates for each tag, which are subsequently utilized in the stereoscopic-vision process to reconstruct the scene in three dimensions.

If the process of obtaining the tag-coordinate package, as shown in Algorithm 1, is successful, the coordinates of all detected points are updated. Otherwise, an estimation process for coordinate positions is executed. This estimation process uses Kalman filters (Kalman, 1960), initialized at a random point and updated at each iteration of the process. This characteristic ensures the proposed methodology's robustness in handling real-time images, which may experience temporary changes in lighting, vibration, or partial or total occlusions of the scene.

After ensuring the stability of the tag coordinates, we proceed to execute computer-vision techniques for stereoscopic vision. This allows us to calculate the projection matrix $\mathbf{P}$, which enables the estimation of the 3D positions of points derived from 2D scenes. The overall process is summarized in the flow diagram in Figure 5.

Algorithm 1 Digital Image Processing

Require: $imagesWithTags$: A set of images containing ARTags
$|imagesWithTags| \geq 2$: At least two images are required

Ensure: $pointsImg$: Ordered points for each detected ARTag

for img in $imagesWithTags$ **do**
  Convert img to grayscale: $gray\_img \leftarrow rgb2gray(img)$
  Apply Gaussian blur: $blur\_img \leftarrow gaussian\_blur(gray\_img)$
  Perform edge detection: $edge\_img \leftarrow Canny(blur\_img)$
  Find contours: $contours \leftarrow FindContours(edge\_img)$
  for $contour$ in $contours$ **do**
    if Contour has 4 vertices ($|contour| == 4$) **then**
      Transform contour to ARTag perspective: $tag\_img \leftarrow WarpPerspec(gray\_img, contour)$
      Decode ARTag ID: $tag\_id \leftarrow DecodeID(tag\_img)$
      if tag_id matches a known tag **then**
        Extract tag location: $tag\_location \leftarrow DecodeLocation(tag\_img)$
        Append to points: $pointsImg \leftarrow OrderedPoints(tag\_location)$
      end if
    end if
  end for
end for

The process of computing the camera projection matrix requires a set of corresponding points $\mathbf{X}_i \leftrightarrow \mathbf{x}_i$ between 3D space points $\mathbf{X}_i$ and their 2D image projections $\mathbf{x}_i$ as input variables. In computer vision, when working with transformations between 3D world coordinates and 2D image coordinates, it is standard practice to use homogeneous coordinates (Ref. (Hartley & Zisserman 2003), Ch. 1). A point in 3D space is represented as a 4-vector:

$$\mathbf{X}_{\mathrm{i}} = (\mathrm{X}_{\mathrm{i}}, \mathrm{Y}_{\mathrm{i}}, \mathrm{Z}_{\mathrm{i}})^{\mathrm{T}} \tag{1}$$

Where the fourth component is introduced to facilitate affine transformations. Similarly, a point in the 2D image space is represented as a 3-vector:

$$\mathbf{x}_{\mathrm{i}} = (\mathrm{x}_{\mathrm{i}}, \mathrm{y}_{\mathrm{i}}, \mathrm{w}_{\mathrm{i}})^{\mathrm{T}} \tag{2}$$

Homogeneous coordinates allow transformations, such as translations and perspective projections, to be represented using matrix multiplication.

The camera projection matrix $\mathbf{P}$ is a 3 × 4 matrix that maps a 3D point in homogeneous coordinates $\mathbf{X}_i$ to a 2D point in homogeneous coordinates $\mathbf{x}_i$ on the image plane. The projection equation is given by:

$$\mathrm{x_i} = \boldsymbol{P}\boldsymbol{X}_\mathrm{i} \tag{3}$$

To compute the projection matrix $\mathbf{P}$, we start by deriving the fundamental relationship between corresponding 3D and 2D points (Ref. (Hartley & Zisserman 2003), Ch. 7). Following the standard formulation, we obtain:

$$\begin{bmatrix} 0^{\mathrm{T}} & -\mathrm{w_i}\mathrm{X_i}^{\mathrm{T}} & \mathrm{y_i}\mathrm{X_i}^{\mathrm{T}} \\ \mathrm{w_i}\mathrm{X_i}^{\mathrm{T}} & 0^{\mathrm{T}} & -\mathrm{x_i}\mathrm{X_i}^{\mathrm{T}} \\ -\mathrm{y_i}\mathrm{X_i}^{\mathrm{T}} & \mathrm{x_i}\mathrm{X_i}^{\mathrm{T}} & 0^{\mathrm{T}} \end{bmatrix} \begin{pmatrix} \mathrm{P}^1 \\ \mathrm{P}^2 \\ \mathrm{P}^3 \end{pmatrix} = 0 \tag{4}$$

Since the three equations in the system above are linearly dependent, only the first two equations are typically used:

$$\begin{bmatrix} 0^{\mathrm{T}} & -\mathrm{w_i}\mathrm{X_i}^{\mathrm{T}} & \mathrm{y_i}\mathrm{X_i}^{\mathrm{T}} \\ \mathrm{w_i}\mathrm{X_i}^{\mathrm{T}} & 0^{\mathrm{T}} & -\mathrm{x_i}\mathrm{X_i}^{\mathrm{T}} \end{bmatrix} \begin{pmatrix} \mathrm{P}^1 \\ \mathrm{P}^2 \\ \mathrm{P}^3 \end{pmatrix} = 0 \tag{5}$$

By stacking the equations for multiple correspondences, a 2n × 12 matrix $\mathbf{A}$ is formed, where n is the number of 3D-2D correspondences. The projection matrix $\mathbf{P}$ is computed by solving the homogeneous system:

$$\boldsymbol{A}\boldsymbol{p} = 0 \tag{6}$$

Where $\boldsymbol{p}$ is the vector containing the elements of the matrix $\boldsymbol{P}$.

It is important to note that both $\mathbf{X}_i$ and $\mathbf{x}_i$ are represented as column vectors, in accordance with the conventions of matrix multiplication used in homogeneous coordinate transformations. The resulting 2D vector $\mathbf{x}_i$ is also in homogeneous form, and its final screen coordinates can be obtained by dividing the x and y components by the third homogeneous coordinate w_i (Ref. (Hartley & Zisserman, 2003), Ch. 1,7).

Algorithm 2 outlines the procedure for computing the camera projection matrix for each camera in the system. This algorithm is responsible for determining the relationship between the 3D coordinates of points in space and their 2D projections on the camera image planes. To achieve this, we use the Direct Linear Transformation (DLT) method, selected for its simplicity and effectiveness in calculating projection matrices from known correspondences between 3D points and 2D image points.

The algorithm begins by correcting lens distortion in the images, a crucial step given the magnifying lenses used in microscopy, which introduce significant radial distortion. The calibration process employs Zhang's calibration method, known for its ability to handle radial and tangential distortions while providing accurate intrinsic and extrinsic camera parameters. This method was selected due to its widespread use in computer-vision applications and its ability to perform well even with a minimal number of calibration images. Once distortion is corrected, the algorithm proceeds to calculate the initial projection matrices using the DLT algorithm, which estimates the matrices by minimizing the geometric reprojection error. This ensures that the calculated matrices provide the best fit for the known correspondence between the ARTag coordinates in the 3D scene and their 2D image positions.

The tuning parameters for the reprojection error minimization were chosen based on the scale and precision required for micrometric measurements. The algorithm iteratively refines the projection matrices by adjusting these parameters to achieve subpixel accuracy in the reconstructed 3D points.

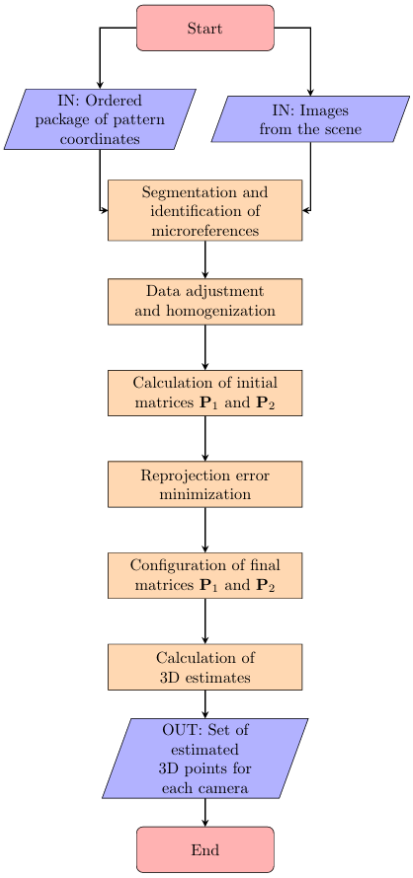

Figure 5. Flowchart for the extraction of depth information and the calculation of camera projection matrices P_1 and P_2.

In summary, this algorithm accurately computes the camera projection matrices, enabling the precise mapping of the 3D scene onto the 2D images, which is fundamental for the stereoscopic reconstruction process.

Algorithm 2 Calculating Camera Projection Matrix

Require: $imagesWithTags$: Images containing ARTags
$cameraMatrix$: Initial camera calibration matrix
$coordPatron$: At least 4 known pattern coordinates

Ensure: P: Projection matrices for each camera

1: Undistort images: $images\_undistorted \leftarrow CorrectDistort(imagesWithTags, cameraMatrix$
2: Detect ARTags: $coord\_tags \leftarrow Algorithm1(images\_undistorted)$
3: Convert tag coordinates to homogeneous form: $coord\_homogeneous \leftarrow alg2hom(coord\_tags, coordPatron)$
4: Compute initial projection matrices using DLT: $initial\_P \leftarrow DLT\_Algorithm(coord\_homogeneous)$
5: Refine matrices by minimizing geometric error: $P \leftarrow Minimize\_Geom\_Error(initial\_P, coord\_homog.)$

3.3 Step 3 — Triangulation of Coincident Points, Partial Reconstruction of the Three-Dimensional Scene, and Estimation of the Microscopy Probe Location

The camera projection matrices $\mathbf{P}_1$ and $\mathbf{P}_2$ returned by the execution of Algorithm 2 allow us to estimate the three-dimensional location of each of the image points $\mathbf{x}_i$ for each camera. This estimation is performed by triangulating the corresponding points in 3D space, reconstructing the scene based on the projections onto the image planes.

The position coordinates of the objects are determined by the structure model and the camera parameters $\mathbf{P}_1$ and $\mathbf{P}_2$. Then, the 3D coordinates $\mathbf{X}_i$ of the target objects relative to the camera coordinate system in 3D space are obtained by solving the system of equations based on the projection matrices and the 2D image points $\mathbf{x}_i$.

The Scale-Invariant Feature Transform (SIFT) algorithm is widely recognized for its ability to detect and describe local features in images, regardless of scale and rotation. In this work, SIFT is used to identify key points in the scene, such as ARTags, by matching features across images from different perspectives. SIFT excels at detecting distinctive, scale-invariant features, making it well-suited for handling microscopic scenes where precise feature matching is critical for accurate 3D reconstruction.

One of the key advantages of SIFT is its robustness to changes in scale, orientation, and even moderate affine transformations, making it highly versatile in various applications. However, SIFT is computationally expensive, particularly when dealing with high-resolution images or large datasets. Its performance may also degrade in real-time applications due to the processing time required for feature extraction and matching. Despite these drawbacks, its accuracy and reliability make it a valuable tool for tasks where precision is essential.

The Speeded-Up Robust Features (SURF) algorithm is a more efficient alternative to SIFT, designed to offer similar performance in feature detection and matching while significantly reducing computational complexity. In this work, SURF is considered for identifying and matching ARTags across images taken from different angles, particularly in scenarios where faster processing times are required without substantially sacrificing accuracy.

SURF's primary advantage is its speed; it uses an integral image representation to compute features more rapidly than SIFT, making it suitable for real-time applications. Additionally, SURF maintains robustness to scale and rotation, although it is less effective at handling significant affine transformations compared to SIFT. A potential disadvantage of SURF is its lower accuracy in complex or textured scenes, as its feature descriptors may not be as distinctive as those of SIFT. Nevertheless, its balance between speed and performance makes it an excellent choice for applications where time constraints are critical.

Since the locations of the two main planes of interest are known in advance, algorithms can be applied to scale the scene to real-world dimensions. This segmentation of the workspace, where the sample for analysis is situated, is crucial because it enables the use of algorithms such as SIFT (Mortensen et al., 2005) and SURF (He et al., 2009) for automatic detection of corresponding points across images within specific regions.

For a more precise estimation of the microscopy probe's location, a design is proposed, as illustrated in Figure 6. In this design, a single tag is positioned on the probe's plane. When this tag is identified in both images, it provides precise coordinates for the probe, enabling more accurate triangulation of the point of interest.

In summary, the selection of computer-vision methods for this work balances the need for accuracy and processing speed. Image segmentation simplifies the scene by isolating areas of interest, improving the efficiency of subsequent analysis steps, but it can be sensitive to noise. SIFT offers unparalleled accuracy in feature detection

and matching, especially for tasks requiring scale and rotation invariance, but its high computational cost makes it less suitable for real-time applications. SURF, on the other hand, sacrifices some accuracy for speed, making it a good compromise when real-time processing is a priority. By combining these methods, the system ensures both precise micrometric measurements and efficient processing, adaptable to the specific requirements of the scanning probe microscopy setup.

3.4 Step 4 - Stepper Motor Control

After identifying the reference points on both the base and the probe within the known workspace, motor commands are issued to reach specific points of interest within the scene and then scan in two or three dimensions as needed. The servo-control algorithm takes the estimated 3D coordinates of the probe tip and translates them into motor commands for the XYZ Cartesian platform. It uses feedback from the stereoscopic vision system to dynamically adjust the probe's position while scanning the sample. The algorithm calculates the necessary movements for each motor and sends control signals to the stepper motor drivers, ensuring precise microstepping. Safety limits are also implemented within the algorithm to avoid exceeding the workspace boundaries, protecting the sample and probe from collisions. Safety parameters are also established to ensure the probe remains within the workspace to prevent accidents.

4. Experiment

In this section, the experimental validation of the proposed method is presented, which involved:
(i) XYZ Cartesian motion platform with stepper motors and microstep drivers.
(ii) Toolbox with a graphical interface, developed in Python 3.
(iii) Computer-vision algorithms for estimating micrometer distances.

Figure 7 shows an implementation of the conceptual scheme (Figure 1) where two standard optical microscopes were used.

The XYZ platform is driven by NEMA 17 motors (57J1880-450-6.35), with their respective controllers (2DM542). These motors are configured for 4000 μ-steps per revolution, which is equivalent to approximately $2\mu m$ per step. For communication and control of the XYZ axial movement platform, an independent microcontrolled system was developed, using a serial communication protocol. This system ensures robust communication and parallel control of devices, meaning that all motors can be active simultaneously, executing their corresponding tasks.

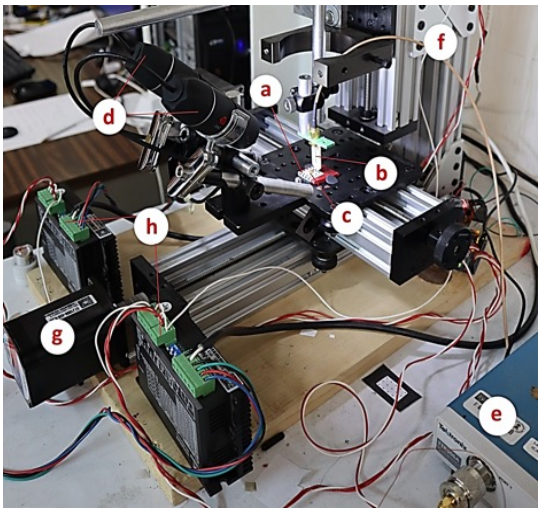

Figure 7. Implementation of a scanning microwave microscope with two optical microscopes. a) Sample holder with tags; b) microscope probe tip; c) sample; d) optical microscopes; e) vector network analyzer (VNA); f) XYZ platform; g) stepper motor; h) stepper motor drivers.

To ensure the accuracy of the XYZ platform's movements, additional validation was performed by measuring the correspondence between the motor steps and the actual displacement of the table. This verification step, conducted using a calibrated micrometer to measure various step sizes, provided further confidence in the precision of the system's movement, confirming that the observed motor steps aligned with the expected displacement on a micrometer scale. These internal checks are critical for ensuring that the results presented in this study are both reliable and repeatable.

For the visual subsystem, two optical microscopes with USB connections were used, with the magnification adjusted to capture images of about 25 *mm* × 20 *mm* at the focal point. These microscopes move with the mobile platform in the X and Y directions and allow constant illumination adjustment over the scene.

The control system, which integrates all components (hardware and software), was developed in Python 3. For user convenience, the visual interface shown in Figure 8 was developed, from which the entire system can be managed. All the implemented software can be found at the following GitHub repository, along with instructions: https://github.com/JorgeMartinez1/Micrometric-Probe-and-Sample-Position-Measurement.git

Figure 8. Visual interface for mechanical control and integration with machine vision, with representative parameters.

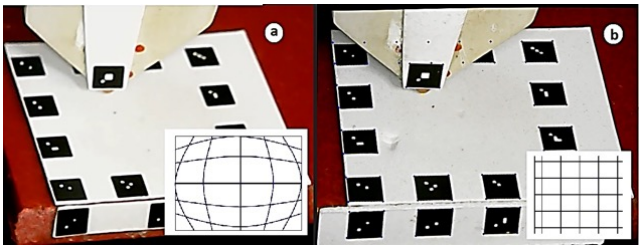

Figure 9. Before and after applying the camera-calibration process. a) Image with radial distortion introduced by the camera lens. b) Image corrected through the camera-calibration process to eliminate radial distortion.

Lens distortion is corrected in the images, as illustrated in Figure 9, ensuring that straight lines appear straight. Furthermore, the calibration-parameter information is stored in a folder specified in the graphical interface.

4.2 Step 2 — Digital Image Processing and Extraction of Depth Information

After focusing the optical microscopes on the scene of interest and obtaining their calibration parameters, an image is captured with each microscope. These two images serve as input parameters for Algorithm 1, which is responsible for processing and extracting, among other things, location information for visible tags. The algorithm returns a collection of ordered correspondences between the two images, where each tag provides four points of interest, as illustrated in Figure 10.

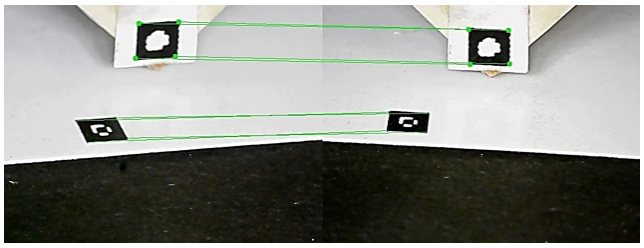

Figure 10. Points of correspondence between images from two cameras captured at different angles.

The experimental validation of the methodology was performed through the following steps:

4.1 Step 1 — Optical Microscope Focusing and Calibration

Because the optical microscopes are fixed to the mobile platform along the X and Y axes—the same platform to which the base with the QR patterns and the sample are fixed—a manual focus can be established. This ensures that, in the scene, the sample holder with the collection of tags is consistently displayed at the bottom reference.

After achieving focus, the camera-calibration process is initiated through the graphical interface. During this process, the user is prompted to specify the number of photographs to capture and the name of the folder for storing these images, along with the calibration parameters. Simultaneously, the microscopy probe needs to be repositioned until it exits the scene, revealing only the stationary calibration tags. To ensure a stable approximation of the cameras' intrinsic parameters, more than 20 photographs are captured, each offering different perspectives of the pattern used by each optical microscope.

Image segmentation is a fundamental process in computer vision that involves partitioning an image into multiple segments to simplify its analysis. In the context of this work, segmentation is applied to identify regions of interest, such as the ARTags used for camera calibration and stereoscopic vision. By isolating these tags from the rest of the scene, the subsequent steps in the pipeline, such as contour detection and tag identification, become more efficient and accurate.

The advantage of image segmentation lies in its ability to reduce the complexity of an image, focusing computational resources on the relevant areas. Additionally, it helps improve the accuracy of object-recognition tasks by providing clearer boundaries between objects. However, segmentation can be sensitive to noise and variations in lighting conditions, which may affect its performance in less controlled environments. The choice of segmentation technique and its parameters must be carefully adjusted based on the specific characteristics of the scene and the objectives of the analysis.

The identified set of coincident points from the images, along with the list of pattern coordinates, is used in

Algorithm 2 to compute the projectivity matrices $\mathbf{P}_1$ and $\mathbf{P}_2$ for the two microscopes in use.

Using the obtained matrices $\mathbf{P}_1$ and $\mathbf{P}_2$, along with the collection of corresponding points between the images, a disparity map is generated, displaying the depth information of the scene, as depicted in Figure 11.

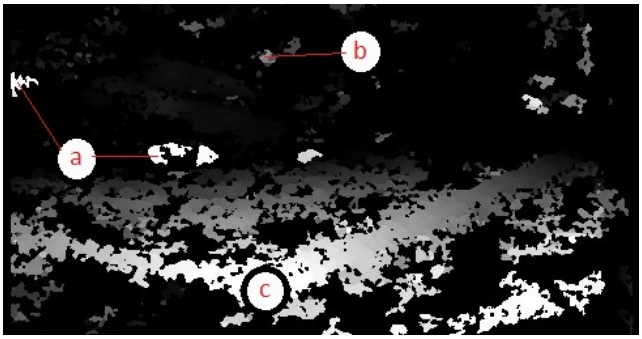

Figure 11. Example of a disparity map between images from two cameras. a) Tags at the sample holder; b) tag at the microscope probe tip; c) sample-holder corner.

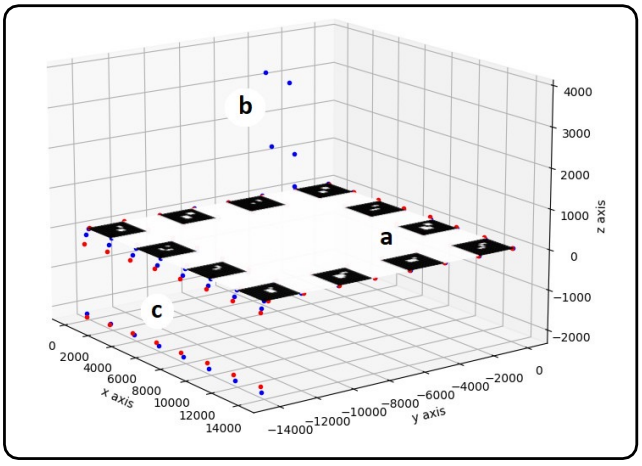

Figure 12. The triangulation process produces a calibrated three-dimensional map of corresponding points between the two microscope images. Each red point represents the known 3D location of the corners of the ARTags, while the blue points depict the estimated locations based on the stereoscopic-vision process. a) Points situated on the plane labeled with the letter 'a' denote the corners of the ARTags on the XY plane of the sample-holder base. b) The five points located on the plane labeled with the letter 'b' represent the four corners of the tag positioned on the microscopy probe, and the lower point is the estimated location of the probe tip. c) Points located on the plane labeled with the letter 'c' signify the corners of the ARTags situated on the XZ plane of the sample-holder base.

4.3 Step 3 — Triangulation of coincident points, partial reconstruction of the three-dimensional scene and estimation of the microscopy probe location.

Applying Algorithm 2, the identified points undergo a triangulation process, ensuring precise measurements in micrometers. Refer to Figure 12 for a visual representation of this triangulation.

Given the known geometry of the probe and the presence of a reference tag on it, an accurate estimation of its position in a three-dimensional scene becomes possible.

5. Results

A set of measurements along the three axes X, Y, Z was performed to characterize the system. The X-axis was scanned over a range of 8000μm, with steps of 10μm in ascending and descending directions. Similarly, the Y-axis was scanned using the same parameters as the X-axis, and the Z-axis was scanned over a range of 4000μm, with steps of 10μm. At each step along each axis, the algorithm described in the previous section was allowed to run and the location estimate of the microwave probe returned by the algorithm was recorded. These positions are represented by the vectors $\mathbf{X}_{a[800]}$, $\mathbf{X}_{d[800]}$, $\mathbf{Y}_{a[800]}$, $\mathbf{Y}_{d[800]}$, $\mathbf{Z}_{a[400]}$, $\mathbf{Z}_{d[400]}$, where the numbers refer to the size of the vectors.

Figure 13 illustrates the datasets obtained for the scanning-probe location as it was scanned along each of the three axes over the ranges mentioned above (blue points). In the first row of graphs, we observe that the position of the probe relative to the sample follows very closely a linear fit to the data (orange points). The correlation coefficient r for the line fit was calculated to be 1.00, indicating a highly linear relationship between the mechanically determined position of the probe and the position measured with the computer-vision approach. The insets in each of the graphs in the first-row show in more detail the data obtained over a range of 300μm. Here, we notice that the deviations from linearity and the noise level of the measurement are not the same for the three axes and are in a range of tens of micrometers.

The second row of Figure 13 shows a histogram of errors associated with the position measurement on each of the three axes (blue points). An estimation of the normal distribution (red line) of the errors indicates the presence of random noise in the measurements. Median error = 0.53 and Std. Error = 11.67 (all values are given in μm). In the second row of Figure 13, the green lines represent the

standard deviations associated with the errors relative to the actual movement. From this, the data indicate that, at one standard deviation, there is an uncertainty of approximately 10μm in the X-axis, 50μm in the Y-axis, and 25μm in the Z-axis. These differences are not surprising given that the position of the two cameras implies that different planes in this coordinate system are projected at different angles in the plane of the image sensor.

This analysis was performed for the datasets $\mathbf{X_d}$[800], $\mathbf{Y_a}$[800], $\mathbf{Y_d}$[800], $\mathbf{Z_a}$[400], and $\mathbf{Z_d}$[400]. The main values of the analysis are summarized in Table 1. Here, we find that the median error is typically a fraction of a micrometer, indicating errors symmetrically distributed above and below the line fit. The standard deviation is on the order of tens of microns, which can be interpreted as an approximate measure of the spatial resolution of the system. We notice that errors vary slightly depending on the direction of movement. For instance, errors along the Y-axis tend to be larger, as it is along this axis that the system exhibits the greatest depth variation.

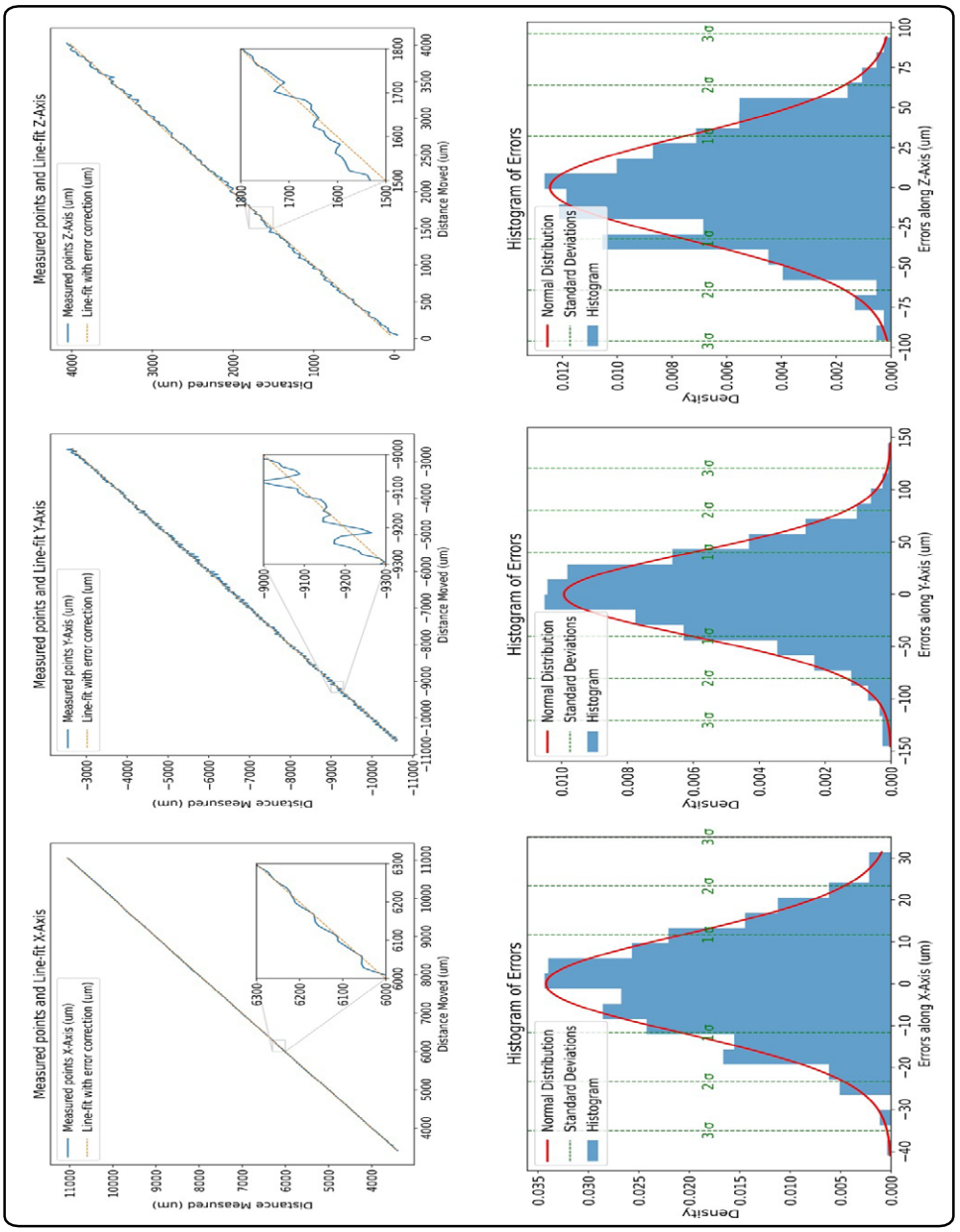

Figure 13. Set of experimental results. The first row contains the moved distance vs. the measured distance for each of the X-, Y-, and Z-axes, and the second row contains error histograms for each of the axes, along with labels illustrating error density at one, two, and three standard deviations.

In comparison to the physical parameters of the system, one standard deviation corresponds to 10μm in the X direction, 50μm in the Y direction, and 25μm in the Z direction. The microscope optics have an image size of 320 × 240 pixels, and each pixel corresponds to 80μm in the image. Therefore, we can observe that the vision system exhibits errors in positions smaller than the pixel size. Here, we assume that the errors inherent in the positioning of the stepper motors and linear stages (i.e., the *Distance Moved* in Figure 13) are much smaller than the measured errors, an assumption that was verified independently. The total time required for each position measurement, including processing, was in the range of 100μs, which is comparable to the data-acquisition time at each pixel of a typical scanning microwave microscope.

Table 1. Analysis of Statistical Errors for `XYZ-Axis` Measurements.

AXIS↑↓	Median Error	Std. Error
X ↑	0.53	11.67
X ↓	-0.03	8.99
Y ↑	0.62	43.58
Y ↓	1.56	40.18
Z ↑	-2.30	30.51
Z ↓	-0.72	32.04

Table values are expressed in μm.

The values obtained from the system demonstrate consistency across multiple trials and applications. The standard for comparison was a physical micrometer with accuracy in the micrometer range. The use of internal references—such as tags of known dimensions within the workspace—provides a reliable means of verifying the accuracy of the measurements.

6. Conclusion

This study introduces a methodology, rooted in computer-vision techniques, for precisely estimating the distance between the probe of a typical scanning probe microscope and the surface of a specimen or sample holder. To validate this methodology, an implementation of a scanning microwave microscope system was augmented with two optical microscopes. The entire probe-sample scene was reconstructed digitally and was used to measure the positions of the probe and the sample holder.

The results demonstrate that through the triangulation process, the measurements surpassed the resolution limits of the optical microscopes. In this case, using cameras with a pixel size corresponding to 80μm at the sample, a spatial resolution of up to 10μm was obtained. These results are obtained in a subsecond timescale, allowing for their use in dynamic measurements. In this particular implementation, we did not use high-resolution cameras. By improving the resolution or magnification of this hardware, this methodology allows for micrometer-scale measurements of probe-sample distances approaching the diffraction limit.

In the implementation of computer vision, we introduce a hybrid process addressing the challenges of camera calibration and minimal correspondences between images. This approach incorporates the use of augmented reality (AR) codes, specifically ARTags, and Kalman filters to ensure the continuity and robustness of the process.

The methodology stands out for its ability to estimate the distance between the probe and the sample, without requiring a very flat sample and without the need for direct contact with the sample's surface.

The precision achieved by the proposed system, while subject to variation depending on specific configurations, is suitable for a range of applications requiring micrometric accuracy. For applications where real-time adjustments and minimal error margins are essential, the system's integration of visual feedback mechanisms and its ability to dynamically recalibrate based on known reference tags ensure that the measurements remain robust. While further validation may be needed for more specialized applications, the current results indicate that the system performs well in environments such as scanning probe microscopy, where precise positioning is crucial.

One factor that influences the accuracy of the measurements is the resolution of the cameras used in the system. Although the current setup, designed to test the measurement scheme, provides precision at the scale of tens of micrometers, increasing the camera resolution can improve the precision of the triangulated measurements. The methodology is designed to be flexible and can accommodate variations in resolution through recalibration procedures using known-dimensional references in the scene.

While this work focuses on the integration of computer-vision techniques and stereoscopic vision for micrometric positioning, it is important to note that other methods, such as laser interferometry, could provide more precise means of measurement. These methods, however, often require more complex setups and can be limited in their flexibility when adapting to dynamic or variable environments, or surfaces with variable topography and optical reflectivity. By contrast, the proposed system, with its reliance on widely available camera technology and visual tags, offers a competitive and accessible

alternative, particularly for applications that prioritize adaptability and lower cost over ultra-high precision.

Inherent in the algorithms is the generation of partial or complete reconstructions of micrometric three-dimensional scenes. This allows for additional applications, including the facilitation of path planning for microscope data capture.

Funding

The authors would like to acknowledge funding from Instituto de Ciencias Aplicadas y Tecnología (ICAT); Universidad Nacional Autónoma de México (UNAM) project PAPIIT IG100521, 101424; D. M. acknowledges financial support from the Spanish Ministry of Science and Innovation through the Ramón y Cajal grant RYC2021-031166-I and Instituto de Magnetismo Aplicado de la Universidad Complutense de Madrid (IMA-UCM).

Conflicts of interest

The authors do not have any type of conflict of interest to declare.

References

Ash, E. A., & Nicholls, G. (1972). Super-resolution aperture scanning microscope. *Nature*, *237*(5357), 510–512. https://doi.org/10.1038/237510a0

Chang, D., Sakuma, S., Kera, K., Uozumi, N., & Arai, F. (2018). Measurement of the mechanical properties of single Synechocystis sp. strain PCC6803 cells in different osmotic concentrations using a robot-integrated microfluidic chip. *Lab on a Chip*, *18*(8), 1241-1249. https://doi.org/10.1039/C7LC01245D

Cyganek, B., & Siebert, J. P. (2011). *An introduction to 3D computer vision techniques and algorithms*. John Wiley & Sons.

Farina, M., Mencarelli, D., Morini, A., Pierantoni, L., Jin, X., & Hwang, J. (2017, July). Developments of microwave microscopy for application to biological samples. In *2017 International Conference on Manipulation, Automation and Robotics at Small Scales (MARSS)* (pp. 1-5). IEEE. https://doi.org/10.1109/MARSS.2017.8001947

Fatikow, S., Eichhorn, V., Krohs, F., Mircea, I., Stolle, C., & Hagemann, S. (2008). Development of automated microrobot-based nanohandling stations for nanocharacterization. *Microsystem Technologies*, *14*(4), 463-474. https://doi.org/10.1007/s00542-007-0471-5

Feenstra, B. J., Vlahacos, C. P., Thanawalla, A. S., Steinhauer, D. E., Dutta, S. K., Wellstood, F. C., & Anlage, S. M. (1998, June). Near-field scanning microwave microscopy: measuring local microwave properties and electric field distributions. In *1998 IEEE MTT-S International Microwave Symposium Digest (Cat. No. 98CH36192)* (Vol. 2, pp. 965-968). IEEE. https://doi.org/10.1109/MWSYM.1998.705152

Golosovsky, M., & Davidov, D. (1996). Novel millimeter-wave near-field resistivity microscope. *Applied physics letters*, *68*(11), 1579-1581. https://doi.org/10.1063/1.116685

Guo, S., Sawamoto, J., & Pan, Q. (2005, August). A novel type of microrobot for biomedical application. In *2005 IEEE/RSJ International Conference on Intelligent Robots and Systems* (pp. 1047-1052). IEEE. https://doi.org/10.1109/IROS.2005.1545314

Hartley, R., & Zisserman, A. (2003). *Multiple view geometry in computer vision*. Cambridge university press.

He, W., Yamashita, T., Lu, H., & Lao, S. (2009, September). Surf tracking. In *2009 IEEE 12th International Conference on Computer Vision* (pp. 1586-1592). IEEE. https://doi.org/10.1109/ICCV.2009.5459360

Hu, B., Liu, W., Gao, C., Zhu, X., & Zheng, D. (2006). Quantitative microscopy of nonlinear dielectric constant using a scanning evanescent microwave microscopy. *Applied physics letters*, *89*(4). https://doi.org/10.1063/1.2234746

Hügli, H., & Mure-Dubois, J. (2006, October). 3D vision methods and selected experiences in micro and macro applications. In *Two-and Three-Dimensional Methods for Inspection and Metrology IV* (Vol. 6382, pp. 47-54). SPIE. https://doi.org/10.1117/12.693635

Imtiaz, A., Wallis, T. M., & Kabos, P. (2014). Near-field scanning microwave microscopy: An emerging research tool for nanoscale metrology. *IEEE Microwave Magazine*, *15*(1), 52-64. https://doi.org/10.1109/MMM.2013.2288711

Jeong, S., Kim, S., Buonocore, J., Park, J., Welsh, C. J., Li, J., & Han, A. (2017). A three-dimensional arrayed microfluidic blood–brain barrier model with integrated electrical sensor array. *IEEE Transactions on Biomedical Engineering*, *65*(2), 431-439. https://doi.org/10.1109/TBME.2017.2773463

Kalman, R. E. (1960). A new approach to linear filtering and prediction problems. https://doi.org/10.1115/1.3662552

Lee, K., Melikyan, H., Babajanyan, A., & Friedman, B. (2010). Near-field microwave microscopy for nanoscience and nanotechnology. In *Scanning Probe Microscopy in Nanoscience and Nanotechnology 2* (pp. 135-171). Berlin, Heidelberg: Springer Berlin Heidelberg.
https://doi.org/10.1007/978-3-642-10497-8_5

Lu, Q., Bai, J., Wang, K., & He, S. (2017). Design, optimization, and realization of a high-performance MOEMS accelerometer from a double-device-layer SOI wafer. *Journal of Microelectromechanical Systems*, *26*(4), 859-869.
https://doi.org/10.1109/JMEMS.2017.2693341

Martinez-Rivas, A., González-Quijano, G. K., Proa-Coronado, S., Séverac, C., & Dague, E. (2017). Methods of micropatterning and manipulation of cells for biomedical applications. *Micromachines*, *8*(12), 347.
https://doi.org/10.3390/mi8120347

Masuda, T., Ukiki, M., Yamagishi, Y., Matsusaki, M., Akashi, M., Yokoyama, U., & Arai, F. (2018). Fabrication of engineered tubular tissue for small blood vessels via three-dimensional cellular assembly and organization ex vivo. *Journal of Biotechnology*, *276*, 46-53.
https://doi.org/10.1016/j.jbiotec.2018.04.003

Mortensen, E. N., Deng, H., & Shapiro, L. (2005, June). A SIFT descriptor with global context. In *2005 IEEE Computer Society Conference on Computer Vision and Pattern Recognition (CVPR'05)* (Vol. 1, pp. 184-190). IEEE.
https://doi.org/10.1109/CVPR.2005.45

Pan, P., Wang, W., Ru, C., Sun, Y., & Liu, X. (2017). MEMS-based platforms for mechanical manipulation and characterization of cells. *Journal of Micromechanics and Microengineering*, *27*(12), 123003.
https://doi.org/10.1088/1361-6439/aa8f1d

Race, C. M., Kwon, L. E., Foreman, M. T., Huang, Q., Inan, H., Kesiraju, S., ... & Cunningham, B. T. (2017). An automated microfluidic assay for photonic crystal enhanced detection and analysis of an antiviral antibody cancer biomarker in serum. *IEEE sensors journal*, *18*(4), 1464-1473.
https://doi.org/10.1109/JSEN.2017.2777529

Sha, X., Sun, H., Zhao, Y., Li, W., & Li, W. J. (2019). A review on microscopic visual servoing for micromanipulation systems: Applications in micromanufacturing, biological injection, and nanosensor assembly. *Micromachines*, *10*(12), 843.
https://doi.org/10.3390/mi10120843

Siegel, P. H. (2021). Microwaves Are Everywhere:"SMM: Nano-Microwaves". *IEEE Journal of Microwaves*, *1*(4), 838-852.
https://doi.org/10.1109/JMW.2021.3106936

Synge, E. (1928). XXXVIII. A suggested method for extending microscopic resolution into the ultra-microscopic region. *The London, Edinburgh, and Dublin Philosophical Magazine and Journal of Science*, *6*(35), 356-362.
https://doi.org/10.1080/14786440808564615

Tabib-Azar, M., Shoemaker, N. S., & Harris, S. (1993). Non-destructive characterization of materials by evanescent microwaves. *Measurement science and technology*, *4*(5), 583.
https://doi.org/10.1088/0957-0233/4/5/007

Tang, B., Baoguo, Y., Fushun, N., & Peijun, H. (2021, April). Review of Near-Field Microwave Microscopy Technology. In *2021 IEEE 6th International Conference on Computer and Communication Systems (ICCCS)* (pp. 263-267). IEEE.
https://doi.org/10.1109/ICCCS52626.2021.9449267

Vlahacos, C. P., Black, R. C., Anlage, S. M., Amar, A., & Wellstood, F. C. (1996). Near-field scanning microwave microscope with 100 μm resolution. *Applied physics letters*, *69*(21), 3272-3274.
https://doi.org/10.1063/1.118033

Wang, Y. G., Reeves, M. E., & Rachford, F. J. (2000). Simultaneous imaging of dielectric properties and topography in a PbTiO 3 crystal by near-field scanning microwave microscopy. *Applied Physics Letters*, *76*(22), 3295-3297.
https://doi.org/10.1063/1.126611

Yoo, Y. K., Duewer, F., Fukumura, T., Yang, H., Yi, D., Liu, S., ... & Xiang, X. D. (2001). Strong correlation between high-temperature electronic and low-temperature magnetic ordering in La 1− x Ca x MnO 3 continuous phase diagram. *Physical Review B*, *63*(22), 224421.
https://doi.org/10.1103/PhysRevB.63.224421

Yu, N., Shi, Q., Nakajima, M., Wang, H., Yang, Z., Huang, Q., & Fukuda, T. (2017, July). Nanomanipulation of a single carbon nanotube for the fabrication of a field-effect transistor. In *2017 IEEE 17th International Conference on Nanotechnology (IEEE-NANO)* (pp. 818-821). IEEE.
https://doi.org/10.1109/NANO.2017.8117322

Zhao, Y., Jia, D., Sha, X., Zhang, G., & Li, W. J. (2018). Determination of the three-dimensional rate of cancer cell rotation in an optically-induced electrokinetics chip using an optical flow algorithm. *Micromachines*, *9*(3), 118.
https://doi.org/10.3390/mi9030118

Zhang, Z. (2002). A flexible new technique for camera calibration. *IEEE Transactions on pattern analysis and machine intelligence*, *22*(11), 1330-1334.
https://doi.org/10.1109/34.888718